Size effect in nanocomposites: XFEM/level set approach and interface element approach

Dang Phong Bach, Delphine Brancherie, Ludovic Cauvin

Version of Record: https://www.sciencedirect.com/science/article/pii/S0168874X19300952
Manuscript_8ba6daf8f60f750c5a29e4b68bc4d033

Size effect in nanocomposites: XFEM/level set approach and Interface element approach

Dang Phong Bach*, Delphine Brancherie and Ludovic Cauvin

Alliance Sorbonne Universités, Université de Technologie de Compiègne, Laboratoire Roberval FRE UTC-CNRS 2012 - Compiègne, France

ARTICLE INFO

Keywords:
Nanocomposite
Size effect
Finite element method
Surface elasticity
Homogenization

ABSTRACT

With the increasing popularity of nanocomposites appears the necessity of the development of efficient modelization procedures. In particular, numerical strategies have to be developed to reproduce and predict the size effect observed on such materials. Usually, the size effect is taken into account by introducing a surface elasticity at the interface between the nano-inclusions and the matrix. Whereas a lot of works have been developed from the analytical point of view, few contributions are related to numerical description and implementation of such surface elasticity in Finite Element codes. In this work, we present a comparative study between two different numerical approaches of the literature namely XFEM [1] and interface element [2]. For a fair comparison, these two approaches have been implemented in the same framework, considering the same element topology. After validation of the implemented strategies, we investigate, in particular, the influence of the homogenization hypothesis in terms of boundary conditions on the computed effective mechanical properties. The comparison in the present work gives an evaluation of the two studied approaches and it is expected to be a good basis to elaborate an optimal numerical computation method.

1. Introduction

Due to their remarkable mechanical behavior for low reinforcement mass fraction (less than 5%) [3], nano-reinforced polymers are increasingly used as structural materials. This interest has induced considerable world-wide research on nanocomposites mechanical behavior. Most of these studies focused mainly on experimental processing and characterization or analytical modeling. The challenge for the modeling of these materials lies in taking into account the size effect induced by the nano-fillers on the macroscopic behavior of the material. This size effect, commonly attributed to local phenomena at the atomic scale, can be interpreted through an increase in the ratio (interface matrix-inclusions) / (volume fraction of inclusions). The local material modifications induced by the reinforcement can be modeled, in the framework of continuum mechanics, by an interphase [4, 5, 6]. However, from the numerical point of view, the interphase model requires a very fine mesh in order to capture the gradient of the fields in the direction of thickness. Due to the very localized material modifications around the inclusions, interface models are commonly considered to handle the behavior of the interphase. Equivalent interface models can be built from interphase models [7, 8, 9] through asymptotic analysis. Depending on the properties of the interphase relatively to the phases in presence, cohesive, coherent or mixed general interface models can be derived. In the present work, the contribution of the interaction between the matrix and the inclusions is modeled through the introduction of a coherent interface defined by a two-dimensional surfacic linear elasticity law [10] resulting in the introduction of surface stress and surface strain tensors. The coherent interface acts like a membrane for which the surface stresses are related to the jump of the traction vector across the surface. The equilibrium of the interface is then determined thanks to the generalized Young-Laplace equation [11].

The coherent interface model has been implemented in different works to estimate the behavior and effective elastic properties of nanocomposites. Most of these studies extended the classical analytical approaches by adding an imperfect interface between the matrix and the inclusions. We can cite here the extended Eshelby's formalism by Sharma and Ganti [12, 13, 14, 15], the extended generalized self-consistent method (GSCM) by Le Quang and He [16], the extended Mori-Tanaka scheme by Duan et al [17] and the extended Hashin-Strikman bound by Brisard et al [8, 18]. The main limitation of all these developments remains on the fact that only spherical or cylindrical inclusions can be considered. A computational approach able to handle inclusions with complex geometries could breakthrough this limitation.

Numerically, two main categories of approaches are considered in the litterature to take into the size effect observed in nanoreinforced materials. Those two types of techniques, namely molecular dynamics, and finite element, are related to different scales of modeling. Classical molecular dynamic (MD) simulations [19, 20, 21] are conducted at the scale of the atomistic interactions between the chains of the polymer material

*Corresponding author
dang-phong.bach@utc.fr (D.P. Bach)

of the matrix and the nano-fillers whereas continuum finite element formulations (FEM) [22, 23, 1, 24, 25] lie in the framework of continuum mechanics and are based on the introduction of a surface elasticity as suggested by Gurtin and Murdoch [10]. Molecular dynamics simulations have the ability to investigate the phenomena occurring at very small length scales where the standard framework of continuum mechanics is no longer valid. Meanwhile, FEM approaches allow to circumvent the high computational cost inherent to molecular dynamics computations while efficiently reproducing surface effects, at least at a phenomenological point of view.

From these motivations, size-dependent mechanical behavior in nanostructured materials has been first treated numerically by introducing a surface element in a standard FEM framework by Gao et al [23]. A standard finite element implementation with interface element accounting for surface elasticity have been lately employed for predicting the degradation of a noncoherent interface in the framework of finite strains in [2, 26]. More recently, we have to mention the contribution of Javili et al in [27, 28] in which, a general imperfect interface has been treated by using an interface element approach. In the context of surface/interface element, Cenanovic et al [29] suggested a formulation allowing to integrate elastic membranes in a finite element formulation, though such an approach has not been applied to the case of nano-reinforced material. Besides, Yvonnet et al [1] proposed to embed surface effects in an eXtended Finite Element Method (XFEM) allowing therefore handle the arbitrary shapes of inhomogeneities by the level set method. XFEM approach was then extended to account simultaneously for surface elastic energy and surface debonding in [30, 31]. To the best of the author's knowledge, standard FEM with surface/interface element and XFEM/level set are two of the most considered approaches in the literature to capture the size effect in nanocomposites. We propose in this paper to compare the efficiency of these two approaches: XFEM/level set and Interface element based approach. In order to make the comparison as fair as possible, the numerical implementation of each approach has been performed with the same data: size of finite element mesh, material properties, Representative Volume Element (RVE). After being validated thanks to several analytical results, the approaches are exploited to investigate the influence of different types of boundary conditions on the effective elastic properties of the nanocomposite.

The paper is organized as follows: in Section 2, we describe the equations governing the problem of a two-phases medium with a coherent interface. In Section 3 the fundamentals and the discretization techniques for XFEM approach and Interface element approach are presented. The numerical results obtained for both formulations are compared and analyzed in Sections 4 and 5. Finally, in Section 6, the original conclusions of this comparative study are presented.

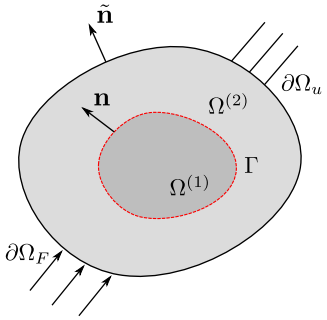

Figure 1: Problem of two phases with an imperfect interface.

2. Problem definition

2.1. Equilibrium equations and boundary conditions

We consider here a continuum body described by a bounded domain $\Omega \subset \mathbb{R}^d$ ($d = 2$ or 3) , with boundary $\partial\Omega$. This domain consists of two-phases $\Omega^{(1)}$ and $\Omega^{(2)}$ (in the following $\Omega^{(1)}$ and $\Omega^{(2)}$ denote inclusion and matrix, respectively). These two phases are partitioned by an interface Γ (see figure 1) with unit normal denoted as $\mathbf{n}$ pointing, conventionally, from $\Omega^{(1)}$ toward $\Omega^{(2)}$. The outward unit normal to $\partial\Omega$ is denoted $\tilde{\mathbf{n}}$. The boundary $\partial\Omega$ is partitioned into $\partial\Omega_u$ where Dirichlet boundary conditions are prescribed and $\partial\Omega_F$ where Neumann boundary conditions hold ($\partial\Omega_F \cup \partial\Omega_u = \partial\Omega$ and $\partial\Omega_F \cap \partial\Omega_u = \varnothing$). In the rest of the paper, the jump of a quantity $\{\bullet\}$ over the interface is defined by $[[\{\bullet\}]] = \{\bullet\}^{(2)} - \{\bullet\}^{(1)}$.

The equilibrium equations in $\Omega^{(i)}$ $(i = 1, 2)$ are given by:

$$\mathbf{div}\boldsymbol{\sigma}^{(i)} + \mathbf{b} = \mathbf{0} \qquad \forall \mathbf{x} \in \Omega^{(i)},\ i = 1, 2\ . \tag{1}$$

The Neumann and Dirichlet boundary conditions on $\partial\Omega$ are defined by:

$$\boldsymbol{\sigma} \cdot \tilde{\mathbf{n}} = \boldsymbol{F} \quad \text{on } \partial\Omega_F \quad \text{and} \quad \mathbf{u} = \bar{\mathbf{u}} \quad \text{on } \partial\Omega_u\ , \tag{2}$$

where $\boldsymbol{\sigma}$ denotes the bulk Cauchy stress tensor and $\mathbf{b}$ denotes a volume force.

As mentioned above, a coherent surface Γ is introduced at the interface between the matrix $\Omega^{(2)}$ and the inclusion $\Omega^{(1)}$. According to the generalized Young-Laplace equation [10] the equilibrium of the interface Γ is given by:

$$\mathbf{div}_s\boldsymbol{\sigma}_s + [[\boldsymbol{\sigma}]] \cdot \mathbf{n} = \mathbf{0} \qquad \forall \mathbf{x} \in \Gamma\ , \tag{3}$$

where $\boldsymbol{\sigma}_s$ is the surface stress tensor and $\mathbf{div}_s$ is the surface divergence operator defined by:

$$\mathbf{div}_s\{\bullet\} = \nabla_s\{\bullet\} : \mathbf{P} \quad \text{with} \quad \mathbf{P} = \mathbf{I} - \mathbf{n} \otimes \mathbf{n}\ , \tag{4}$$

where $\mathbf{I}$ is the second order unit tensor, $\mathbf{P}$ the second order projection operator on the interface Γ and ∇_s the surface gradient.

Moreover, we can mention that contrary to classical continuum mechanics hypothesis, the generalized Young-Laplace equation allows a jump of the traction across the interface Γ. We consider in this paper that there is no decohesion at the interface Γ so that we have the following kinematic conditions (derived from Hadamard's compatibility conditions):

$$\begin{cases} [[\mathbf{u}]] = \mathbf{0} \ , \\ [[\boldsymbol{\epsilon}]] = (\mathbf{a} \otimes \mathbf{n} + \mathbf{n} \otimes \mathbf{a})^s \qquad \mathbf{a} \in \mathbf{R}^d \ . \end{cases} \tag{5}$$

The weak form associated with equations (1) and (3) is given by testing with vector value test functions $\delta\mathbf{u} \in \mathcal{H}^1(\Omega)$ and $\delta\mathbf{u}_s \in \mathcal{H}^1(\Gamma)$ where $\mathcal{H}^1$ denotes the Sobolev space of order 1:

$$\begin{aligned} &\int_\Omega \delta\mathbf{u} \cdot (\mathbf{div}\boldsymbol{\sigma} + \mathbf{b}) \, d\Omega \\ &+ \int_\Gamma \delta\mathbf{u}_s \cdot (\mathbf{div}_s\boldsymbol{\sigma}_s + [[\boldsymbol{\sigma}]] \cdot \mathbf{n}) \, d\Gamma = \mathbf{0} \quad \forall(\delta\mathbf{u}, \delta\mathbf{u}_s). \end{aligned} \tag{6}$$

Using the divergence theorems and taking into account the symmetry of both the bulk and surface stress tensors $\boldsymbol{\sigma}$ and $\boldsymbol{\sigma}_s$, equation (6) can be alternatively written as:

$$\begin{aligned} &\int_{\Omega\setminus\Gamma} (\nabla^s\delta\mathbf{u}) : \boldsymbol{\sigma} d\Omega - \int_{\Omega\setminus\Gamma} \delta\mathbf{u} \cdot \mathbf{b} d\Omega \\ &- \int_{\partial\Omega} \delta\mathbf{u} \cdot (\boldsymbol{\sigma} \cdot \tilde{\mathbf{n}}) dS + \int_\Gamma \delta\mathbf{u} \cdot [[\boldsymbol{\sigma}]] \cdot \mathbf{n} d\Gamma \\ &+ \int_\Gamma (\nabla^s_s\delta\mathbf{u}_s) : \boldsymbol{\sigma}_s d\Gamma - \int_\Gamma \delta\mathbf{u}_s \cdot [[\boldsymbol{\sigma}]] \cdot \mathbf{n} d\Gamma \\ &- \int_{\partial\Gamma} \delta\mathbf{u}_s \cdot (\boldsymbol{\sigma}_s \cdot \mathbf{m}) dl = \mathbf{0} \ , \end{aligned} \tag{7}$$

where we explicitly took into account the jump of the stress tensor $\boldsymbol{\sigma}$ over the interface Γ.

In equation (7), we denoted as ∇^s_s the surfacic symmetric gradient operator (defined as $\nabla^s_s\{\bullet\} = \nabla^s\{\bullet\}\mathbf{P}$), $\partial\Gamma$ is the boundary of Γ and $\mathbf{m}$ is outward unit normal vector to $\partial\Gamma$. In the following, we will assume that the interface Γ is closed so that the term $\int_{\partial\Gamma}$ disappears. Moreover, as already started previously we assume no decohesion at the interface so that we have $\delta\mathbf{u}_s = \delta\mathbf{u}_{|\Gamma}$. Thus, equation (7) can be written as:

$$\begin{aligned} &\int_{\Omega\setminus\Gamma} \nabla^s\delta\mathbf{u} : \boldsymbol{\sigma} d\Omega + \int_\Gamma \nabla^s_s\delta\mathbf{u}_{|\Gamma} : \boldsymbol{\sigma}_s d\Gamma \\ &- \int_{\Omega\setminus\Gamma} \delta\mathbf{u} \cdot \mathbf{b} d\Omega - \int_{\partial\Omega} \delta\mathbf{u} \cdot \boldsymbol{\sigma} \cdot \tilde{\mathbf{n}} dS = \mathbf{0} \ . \end{aligned} \tag{8}$$

2.2. Constitutive equations for the bulk and the interface

The bulk constitutive law in the context of linear elastic model is given by:

$$\boldsymbol{\sigma} = \mathbb{C}^{(i)} : (\boldsymbol{\epsilon} - \boldsymbol{\epsilon}^*) \ , \tag{9}$$

where $\mathbb{C}^{(i)}$ is the fourth-order elastic stiffness tensor associated with domain $\Omega^{(i)}$ and $\boldsymbol{\epsilon}^*$ is a potential/optional eigenstrain prescribed on $\Omega^* \subset \Omega^{(i)}$. On the interface, the surface tangent stress $\boldsymbol{\sigma_s}$ is related to the surface elastic strain tensor $\boldsymbol{\epsilon_s}$ by the following equation which has been presented by Bottomley et al in [32] like a constitutive equation:

$$\boldsymbol{\sigma}_s = \mathbb{C}^s : \boldsymbol{\epsilon}_s \ , \tag{10}$$

where $\mathbb{C}^s$ is the surface stiffness tensor. The interface strain tensor $\boldsymbol{\epsilon}_s$ can be derived from the bulk strain tensor $\boldsymbol{\epsilon}$ by projection on the tangent plane of the interface through the projection operator $\mathbf{P}$ defined in (4):

$$\boldsymbol{\epsilon}_s = \mathbf{P}\boldsymbol{\epsilon}\mathbf{P} \ . \tag{11}$$

For an elastically isotropic surface/interface, the constitutive equation (10) can be rewritten

$$\boldsymbol{\sigma}_s = 2\boldsymbol{\mu}_s\boldsymbol{\epsilon}_s + \boldsymbol{\lambda}_s(\mathrm{tr}\boldsymbol{\epsilon}_s)\mathbf{I} \ , \tag{12}$$

where $\boldsymbol{\lambda}_s$ and $\boldsymbol{\mu}_s$ are Lame's constant for the surface (interface). Taking into account the constitutive relations (9) and (10) and the fact that usually test functions are chosen equal to zero on the Dirichlet boundary $\partial\Omega_u$, the weak form (8) can be expressed as:

$$\begin{aligned} &\int_{\Omega\setminus\Gamma} \boldsymbol{\epsilon}(\delta\mathbf{u}) : \mathbb{C} : \boldsymbol{\epsilon}(\mathbf{u}) d\Omega + \int_\Gamma \boldsymbol{\epsilon}_s(\delta\mathbf{u}_s) : \mathbb{C}^s : \boldsymbol{\epsilon}_s(\mathbf{u}_s) d\Gamma \\ &= \int_{\Omega\setminus\Gamma} \delta\mathbf{u} \cdot \mathbf{b} d\Omega + \int_{\partial\Omega_F} \delta\mathbf{u} \cdot \mathbf{F} d\Gamma \\ &\qquad + \int_{\Omega\setminus\Gamma} \boldsymbol{\epsilon}(\delta\mathbf{u}) : \mathbb{C} : \boldsymbol{\epsilon}^* d\Omega \ , \end{aligned} \tag{13}$$

where $\boldsymbol{\epsilon}\{\bullet\} = \nabla^s\{\bullet\}$ and $\boldsymbol{\epsilon}_s\{\bullet\} = \nabla^s_s\{\bullet\}$. Finally, if the relation (11) is taken into account, we obtain:

$$\begin{aligned} &\int_{\Omega\setminus\Gamma} \boldsymbol{\epsilon}(\delta\mathbf{u}) : \mathbb{C} : \boldsymbol{\epsilon}(\mathbf{u}) d\Omega \\ &\qquad + \int_\Gamma \mathbf{P}\boldsymbol{\epsilon}(\delta\mathbf{u})\mathbf{P} : \mathbb{C}^s : \mathbf{P}\boldsymbol{\epsilon}(\mathbf{u})\mathbf{P} d\Gamma \\ &= \int_{\Omega\setminus\Gamma} \delta\mathbf{u} \cdot \mathbf{b} d\Omega + \int_{\partial\Omega_F} \delta\mathbf{u} \cdot \mathbf{F} d\Gamma \\ &\qquad + \int_{\Omega\setminus\Gamma} \boldsymbol{\epsilon}(\delta\mathbf{u}) : \mathbb{C} : \boldsymbol{\epsilon}^* d\Omega \ . \end{aligned} \tag{14}$$

The next sections of this paper aim at comparing two different implementations of an elastic interface namely XFEM [1] and an approach based on interface element [23]. The two previous equivalent versions of the weak form of the equilibrium equations (13) and (14) serve, respectively, as basis for interface element discretization and XFEM discretization. Indeed, as presented in the next section, the major difference between the two approaches is the explicit (interface element approach) or implicit (XFEM approach) discretization of the displacement along the interface Γ.

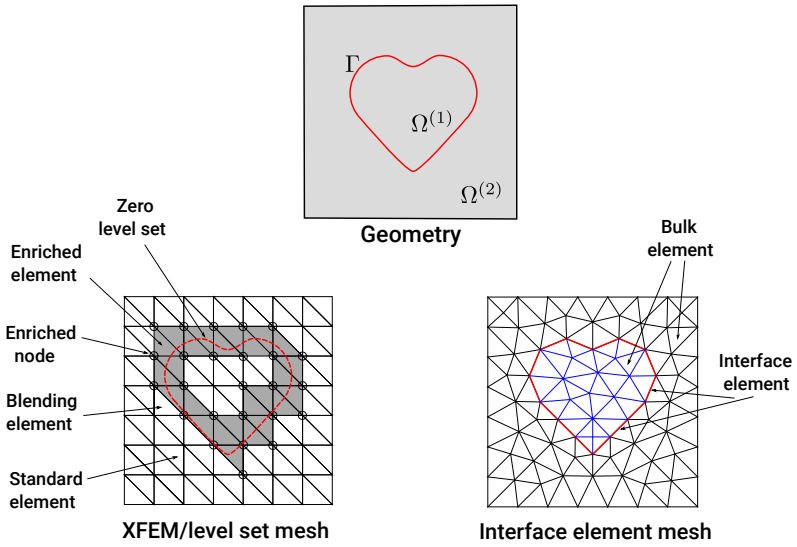

Figure 2: An example of XFEM mesh and Interface element mesh.

3. Finite element implementation

In this work, we limit our investigation to three nodes triangular elements. In the following, we discuss the choices in terms of interpolations and numerical implementation for two different numerical descriptions of the kinematics of the interface, namely XFEM/level set and standard FEM with interface elements. For XFEM/level set approach, the interface is implicitly described by the introduction of a level-set function. Thus, regular meshes can be adopted even if the interface has a complex geometry. On the contrary, for the interface element approach, the interface is explicitly described through a conforming mesh (see figure 2). In both cases, the strain and stress tensor can be expressed in the vector forms:

$$\begin{aligned} \boldsymbol{\epsilon} &= \left[\begin{array}{cccc} \boldsymbol{\epsilon}_{11} & \boldsymbol{\epsilon}_{22} & \eta\boldsymbol{\epsilon}_{33} & 2\boldsymbol{\epsilon}_{12} \end{array} \right]^T , \\ \boldsymbol{\sigma} &= \left[\begin{array}{cccc} \boldsymbol{\sigma}_{11} & \boldsymbol{\sigma}_{22} & \eta\boldsymbol{\sigma}_{33} & \boldsymbol{\sigma}_{12} \end{array} \right]^T , \end{aligned} \tag{15}$$

where, for plane strain problems $\eta = 0$ and the indices 1,2,3 are associated with respectively directions e_x, e_y, and e_z while for axisymmetric problems $\eta = 1$ and the indices 1,2,3 are associated with directions e_r, e_z and e_θ .

3.1. XFEM/levelset approach

For XFEM approach, the specific shape of the interface is defined by means of the introduction of a level set function $\phi(\mathbf{x})$. By denoting $\mathbf{x}^c$ and r^c the center and radius of the inclusion (in the case we consider a circular inclusion), the interface Γ is geometrically defined by:

$$\phi(\mathbf{x}) = \|\mathbf{x} - \mathbf{x}^c\| - r^c = 0 \, , \tag{16}$$

Usually, function $\phi(\mathbf{x})$ is chosen as the signed distance to the interface Γ. With such a choice, the sign of function $\phi(\mathbf{x})$ also defines the partition of the domain into two different phases : $\phi(\mathbf{x}) > 0$ in the matrix and $\phi(\mathbf{x}) < 0$ in the inclusion. The implicit interface is not discretized and we can not derive directly the surface strain tensor $\boldsymbol{\epsilon}_s$. In this case, equation (11) is used to extract the surface strain tensor which implies to form the projection operator $\mathbf{P} = \mathbf{I} - \mathbf{n} \otimes \mathbf{n}$ by numerically evaluating $\mathbf{n}$. This is achieved by considering the discretized form ϕ^h of the level set function $\phi(\mathbf{x})$:

$$\phi^h(\mathbf{x}) = \sum_{i=1}^{n} \mathbf{N}_i \phi_i \, . \tag{17}$$

where $\mathbf{N}_i$ is the finite element shape function associated with node i and $\phi_i = \phi(\mathbf{x}_i)$ where $\mathbf{x}_i$ corresponds to node i. Therefore, the numerical evaluation of $\mathbf{n}$ gives :

$$\mathbf{n}(\mathbf{x}) = \frac{\nabla\phi(\mathbf{x})}{||\nabla\phi(\mathbf{x})||} \, , \tag{18}$$

To satisfy the discontinuous conditions (5) across the interface within the framework of XFEM, the enriched approximation proposed in [33] is used. This approximation is defined at a given point $\mathbf{x} \in \Omega_e$ by:

$$\mathbf{u}^h(\mathbf{x}) = \sum_{i=1}^{n} \mathbf{N}_i(\mathbf{x})\mathbf{u}_i + \sum_{j=1}^{m} \mathbf{N}_j(\mathbf{x})\psi(\mathbf{x})\mathbf{a}_j \, , \tag{19}$$

where the index j corresponds to the set of nodes pertaining to the elements whose support are cut by the interface and $\psi(\mathbf{x})$ is the enrichment function which is defined as [33] :

$$\psi(\mathbf{x}) = \sum_{i=1}^{n} |\phi_i| \mathbf{N}_i(\mathbf{x}) - \left| \sum_{i=1}^{n} \phi_i \mathbf{N}_i(\mathbf{x}) \right| \, . \tag{20}$$

It has to be noticed that this enrichment function has zero values on the nodes of the enriched elements, sug-

gesting that a local enrichment could be proposed instead of a global one.

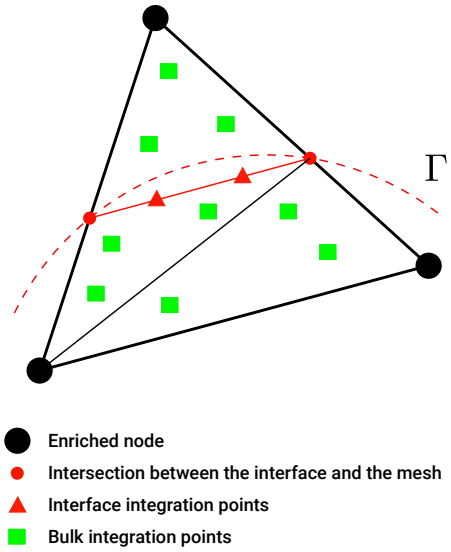

Figure 3: Element cut by the interface Γ, approximated interface and integration points.

In order to compute the surface integral in the weak form (14), a two Gauss points integration is performed along the interface. Note that the geometry of the interface is discretized according to the discretization of the level set function $\phi(\mathbf{x})$ resulting in a piecewise linear approximation of the interface when considering linear finite element interpolation. For the bulk, the elements crossed by the interface are divided into sub-triangles where the numerical integration is carried out considering three integration points (see figure 3). It has to be noticed that, due to the enrichment (see (19)), the interpolation of strains and stresses in the element crossed by the interface is one order higher than for standard elements. Finally, by using the approximation (19), the following discrete system of linear equations is obtained:

$$(\mathbf{K}+\mathbf{K^s})\mathbf{d}=\mathbf{f}\ , \tag{21}$$

where

$$\begin{aligned}
\mathbf{K} = &\int_{\Omega^{(1)}} \mathbf{B}^T\mathbf{C}^{(1)}\mathbf{B}\gamma d\Omega + \int_{\Omega^{(2)}} \mathbf{B}^T\mathbf{C}^{(2)}\mathbf{B}\gamma d\Omega\ ,\\
\mathbf{f} = &\int_{\Omega} \mathbf{N}^T\mathbf{b}\gamma d\Omega + \int_{\partial\Omega_F} \mathbf{N}^T\mathbf{F}\gamma d\Gamma\\
&+ \int_{\Omega^{(1)}} \mathbf{B}^T\mathbf{C}^{(1)}\boldsymbol{\epsilon}^{*(1)}\gamma d\Omega\\
&+ \int_{\Omega^{(2)}} \mathbf{B}^T\mathbf{C}^{(2)}\boldsymbol{\epsilon}^{*(2)}\gamma d\Omega\ ,\\
\mathbf{K^s} = &\int_{\Gamma} \mathbf{B}^T\mathbf{M}^T\mathbf{C}^{(s)}\mathbf{M}\mathbf{B}\gamma d\Gamma.
\end{aligned} \tag{22}$$

and $\mathbf{d}$ gathers all the degrees of freedom:

$$\mathbf{d}=[\mathbf{u}_1...\mathbf{u}_n\ \mathbf{a}_1...\mathbf{a}_m]^T\ . \tag{23}$$

$\gamma = 1$ for plane strain problems and $\gamma = 2\pi r$ for axisymmetric problems. $\mathbf{C}^{(1)}$, $\mathbf{C}^{(2)}$,$\mathbf{C}^{(s)}$ correspond respectively to the matrix form of the elastic tensor for phase (1), phase (2) and the interface Γ.

$$\mathbf{C}^{(i)}=\begin{bmatrix}(\lambda^{(i)}+2\mu^{(i)}) & \lambda^{(i)} & \eta\lambda^{(i)} & 0\\ \lambda^{(i)} & (\lambda^{(i)}+2\mu^{(i)}) & \eta\lambda^{(i)} & 0\\ \eta\lambda^{(i)} & \eta\lambda^{(i)} & \eta(\lambda^{(i)}+2\mu^{(i)}) & 0\\ 0 & 0 & 0 & \mu^{(i)}\end{bmatrix} \tag{24}$$

The matrix $\mathbf{B}$ is defined by $\mathbf{B}=[\mathbf{B}_1\cdots\mathbf{B}_n\hat{\mathbf{B}}_1\cdots\hat{\mathbf{B}}_m]$ with $\mathbf{B}_i=\mathbf{L}(N_i)$ ($\mathbf{L}$ is the standard matrix form of the symmetric gradient operator) and $\hat{\mathbf{B}}_j=\mathbf{L}(N_j\psi)$.

The matrix $\mathbf{M}$ is defined according to:

$$\mathbf{M}=\begin{bmatrix}P_{11}^2 & P_{12}^2 & 0 & P_{11}P_{12}\\ P_{12}^2 & P_{22}^2 & 0 & P_{12}P_{22}\\ 0 & 0 & \eta & 0\\ 2P_{11}P_{12} & 2P_{12}P_{22} & 0 & (P_{12}^2+P_{11}P_{22})\end{bmatrix}. \tag{25}$$

We can note that the introduction of the surface elasticity on the interface Γ results in the introduction of an added stiffness $\mathbf{K}^s$ in the tangential direction of the interface in the resulting linear system of equations.

3.2. Interface element approach

The other strategy explored in that paper to account for a coherent interface is based on an explicit discretization of the interface (see figure 2) through the use of interface elements with surface elasticity. This strategy had been detailed by [2, 27, 34] in the framework of finite strains and in the general case of the imperfect interface where both tractions and displacements can be discontinuous across the interface. We develop here a similar strategy in the framework of small strains and focus only on the treatment of the surface elasticity so that no decohesion is, at that stage, taken into account. In that case, we consider the classical interpolation of the displacement in the bulk given as:

$$\mathbf{u}^h(\mathbf{x})=\sum_{i=1}^{n}\mathbf{N}_i(\mathbf{x})\mathbf{u}_i\ , \tag{26}$$

along with a specific interpolation for the displacement on the interface:

$$\mathbf{u}_s^h(\mathbf{x})=\sum_{i=1}^{m}\bar{\mathbf{N}}_i(\mathbf{x})\mathbf{u}_{s,i}\ , \tag{27}$$

where $\bar{\mathbf{N}}_i$ is the shape function of 1D interface elements associated to node i and $\mathbf{u}_{s,i}$ corresponds to the displacements of node i along the interface direction obtained by projection the components of the displacement in the global frame onto the local frame (see figure 4):

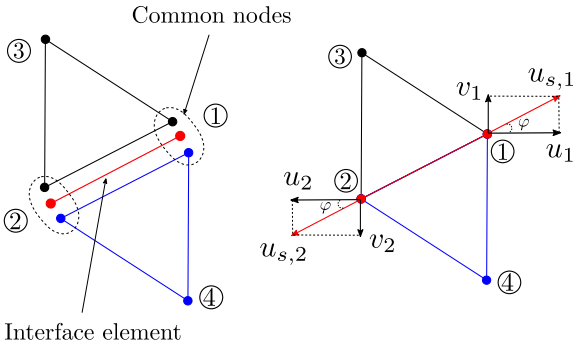

Figure 4: Interface element and bulk neighbor elements.

$$\begin{bmatrix} u_{s,1} \\ u_{s,2} \end{bmatrix} = \underbrace{\begin{bmatrix} \cos\varphi & \sin\varphi & 0 & 0 \\ 0 & 0 & \cos\varphi & \sin\varphi \end{bmatrix}}_{\mathbf{T}} \begin{bmatrix} u_1 \\ v_1 \\ u_2 \\ v_2 \end{bmatrix}, \tag{28}$$

The surface strain tensor in element e is then built such that:

$$\boldsymbol{\epsilon}_s^{(e)} = \bar{\mathbf{B}}^{(e)}\mathbf{T}\mathbf{u} \quad , \tag{29}$$

where $\bar{\mathbf{B}}^{(e)}$ is the matrix of shape function derivatives of a classic 1D element. By using the weak form (13) and the approximations (26) and (27), we obtain the following discrete system of linear equations:

$$(\mathbf{K} + \mathbf{K}^{\mathbf{s}})\mathbf{d} = \mathbf{f} \quad , \tag{30}$$

where

$$\begin{aligned} \mathbf{K} = & \int_{\Omega^{(1)}} \mathbf{B}^T\mathbf{C}^{(1)}\mathbf{B}\gamma d\Omega + \int_{\Omega^{(2)}} \mathbf{B}^T\mathbf{C}^{(2)}\mathbf{B}\gamma d\Omega \, , \\ \mathbf{f} = & \int_{\Omega} \mathbf{N}^T\mathbf{b}\gamma d\Omega + \int_{\partial\Omega_F} \mathbf{N}^T\mathbf{F}\gamma d\Gamma \\ & + \int_{\Omega^{(1)}} \mathbf{B}^T\mathbf{C}^{(1)}\boldsymbol{\epsilon}^{*(1)}\gamma d\Omega \\ & + \int_{\Omega^{(2)}} \mathbf{B}^T\mathbf{C}^{(2)}\boldsymbol{\epsilon}^{*(2)}\gamma d\Omega \, , \\ \mathbf{K}^s = & \int_{\Gamma} \mathbf{T}^T\bar{\mathbf{B}}^T\mathbf{C}^s\bar{\mathbf{B}}\mathbf{T}\gamma d\Gamma \, , \end{aligned} \tag{31}$$

where the surface stiffness matrix is, in this case with the interface element, defined as:

$$\mathbf{C}^s = \begin{bmatrix} \lambda_s + 2\mu_s & \eta\lambda_s \\ \eta\lambda_s & \eta(\lambda_s + 2\mu_s) \end{bmatrix}. \tag{32}$$

4. Numerical results: comparison and analysis

In this section, we compare the performance and results obtained from the two previously presented approaches for different problems. It's worth pointing out that with current technologies, there is no possibility of direct measurement of the mechanical properties of the interface. This limitation has been circumvented in recent works by appealing to molecular dynamics computations for inverse identification of mechanical properties of the interface [35]. The purpose of this article is to compare the performance of two numerical approaches. Therefore the mechanical parameters of the interface, the matrix and the inclusions are not chosen from real materials but to assess the sensibility and robustness of the considered numerical strategies to the problem parameters.

In order to compare the two considered numerical approaches, we handle the problem of a cell with a cylindrical inclusion by considering plane strain hypothesis. A representation of the geometry of the considered problem is given on Figure 5. To evaluate the performance of the two numerical approaches as regards the problem parameters, we vary the mechanical properties of the interface, the matrix, and the inclusion. To that purpose, we define the two "contrast" coefficients α and β:

$$\alpha = \frac{\hat{\kappa}_s}{\hat{\kappa}_m} \qquad \text{and} \qquad \beta = \frac{E_i}{E_m} \, , \tag{33}$$

where $\hat{\kappa}_s = \lambda_s + 2\mu_s$ is the plane strain surface modulus of the interface and $\hat{\kappa}_m$ denotes plane strain bulk modulus of the matrix. E_i and E_m denote the Young modulus of the inclusions and the matrix, respectively.

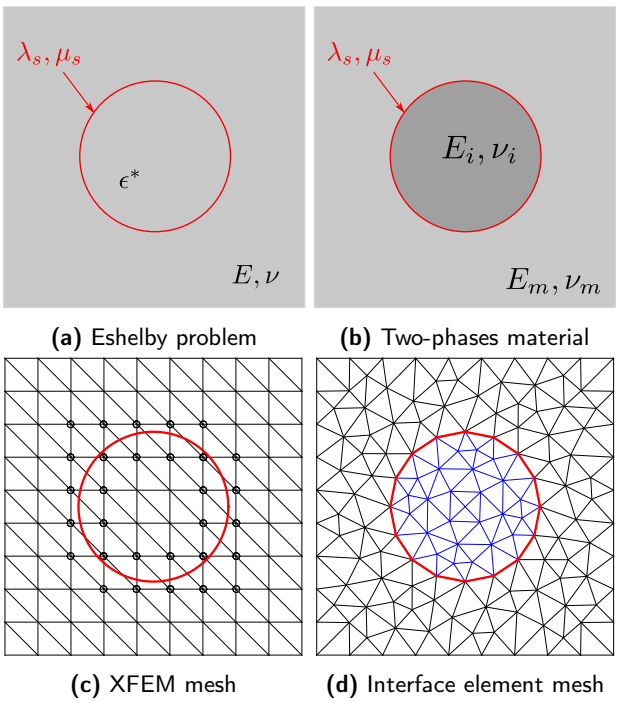

(a) Eshelby problem **(b)** Two-phases material

(c) XFEM mesh **(d)** Interface element mesh

Figure 5: Problems with coherent interface are treated in the plane strain model.

4.1. Validation of the numerical approaches

We first consider the problem of an inclusion immersed in an infinite elastic domain and submitted to a dilatational eigenstrain (see figure 5a). Such a problem corresponds to the so-called Eshelby problem for which analytical solutions including the effect of a coherent interface between the inclusion and the matrix have been derived [12, 13, 14, 15]. For the numerical computation, only a bounded domain is considered around the inclusion and the analytical solution in terms of displacements is prescribed on the boundary of the finite domain. In the results presented in this section, the loading conditions correspond to a dilational eigenstrain $\boldsymbol{\epsilon}^*$ prescribed to the inclusion and such that $\boldsymbol{\epsilon}^* = \boldsymbol{\epsilon}^*_{11} = \boldsymbol{\epsilon}^*_{22} = 0.5, \boldsymbol{\epsilon}^*_{33} = 0$.

The performance of the numerical approaches considered in this paper will be evaluated through the evaluation of the error and rate of convergence, which is performed on the basis of the relative energy norm error defined by:

$$e = \sqrt{\frac{\int_\Omega (\boldsymbol{\epsilon}^h(\mathbf{x}) - \boldsymbol{\epsilon}(\mathbf{x})) : \mathbb{C} : (\boldsymbol{\epsilon}^h(\mathbf{x}) - \boldsymbol{\epsilon}(\mathbf{x}))\, \mathrm{d}\Omega}{\int_\Omega \boldsymbol{\epsilon} : \mathbb{C} : \boldsymbol{\epsilon} \mathrm{d}\Omega}} \tag{34}$$

where $\boldsymbol{\epsilon}^h$ is the computed strain with the considered numerical strategy and $\boldsymbol{\epsilon}$ is the analytical solution. All the computations are performed considering three-node triangular elements and the error is computed for various element sizes h. The results are presented on figure 6. As seen on figure 6a, the introduction of a surface elasticity ($\alpha \neq 0$) degrades the rate of convergence of XFEM. For $\alpha = 0$ (no surface elasticity), the expected rate of convergence $r \approx 1$ is recovered. On the contrary, when considering interface elements, the rate of convergence is not affected by the introduction of surface elasticity and we observe, as expected, a rate of convergence close to 1 for all values of α.

Next, in order to validate the efficiency of the two implemented strategies in reproducing the size effect observed when considering surface elasticity, we compute a size effect indicator defined as follows [1]:

$$\xi = \frac{|\mathbf{E}_s|}{|\mathbf{E}_s| + |\mathbf{E}_b|} = \frac{|\int_\Gamma \boldsymbol{\sigma}_s : \boldsymbol{\epsilon}_s \mathrm{d}\Gamma|}{|\int_\Gamma \boldsymbol{\sigma}_s : \boldsymbol{\epsilon}_s \mathrm{d}\Gamma| + |\int_\Omega \boldsymbol{\sigma} : \boldsymbol{\epsilon} \mathrm{d}\Omega|} \tag{35}$$

where $\mathbf{E}_s$ and $\mathbf{E}_b$ denote the surface and bulk energy respectively. We consider 40×40 nodes mesh for both numerical approaches and compute the size effect indicator ξ for the same volume fraction of inclusion $f = 0.2$ but with various radii of the inclusions and various values of the contrast parameter α. The results are given on figure 7.

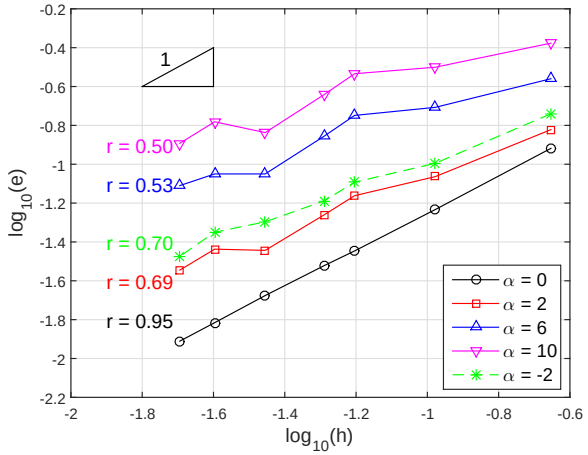

(a) XFEM

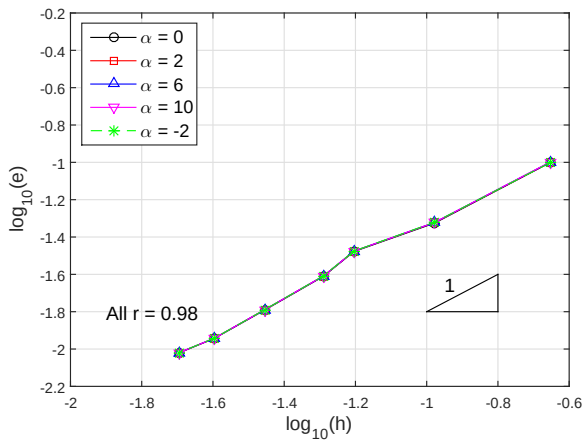

(b) Interface element

Figure 6: Convergence analysis for the extended Eshelby problem ($\beta = 1$) with a coherent interface.

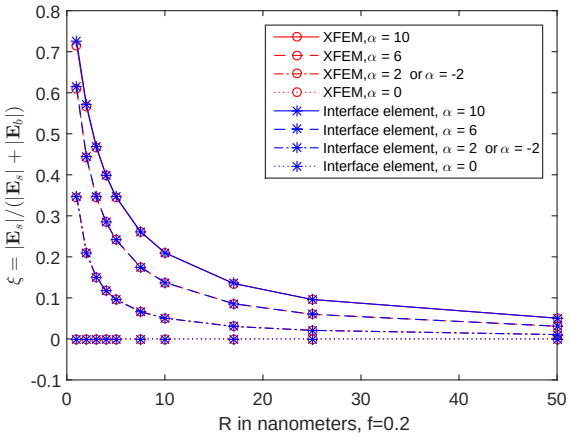

Figure 7: Size effect indicator versus inclusion radius for the extended Eshelby problem ($\beta = 1$).

We can see that the results are quite similar, both numerical approaches are capable of reproducing the expected size effect, though, as mentioned above, the convergence of XFEM is slower than interface element for high values of α.

4.2. Size dependence of effective properties of two-phases nanocomposites

The two implemented numerical strategies can be used to derive, numerically, the effective or homogenized properties of materials presenting nano-inclusions (see figure 5b). The effective bulk modulus and effective shear modulus $(\kappa^s_{eff}, \mu^s_{eff})$ of the nanocomposites differ from those predicted classically with no effect of the interface $(\kappa_{eff}, \mu_{eff})$. These differences $(\kappa^s_{eff} - \kappa_{eff})/\kappa_{eff}$ and $(\mu^s_{eff} - \mu_{eff})/\mu_{eff}$ depend, for a given volume fraction of inclusion f, on the size of the inclusions. In this subsection, we vary the value of the contrast parameter β from 0 (porous material) to 10 to assess how the stiffness contrast ratio of the two materials (matrix and inclusion) affects the size effect, the elastic properties of the interface remaining unchanged. The results are reported on figure 8 for the bulk modulus and on figure 9 for the shear modulus.

For instance, for inclusions 10 times stiffer than the matrix, the effective modulus is not much affected by the size of the inclusions while for nanoporous materials ($\beta = 0$) the size effect is more pronounced. It is worth mentioning that for the purpose of this sensitivity analysis we assumed that the elastic properties of the interface are independent of the elastic properties of the surrounding materials (matrix and inclusion).

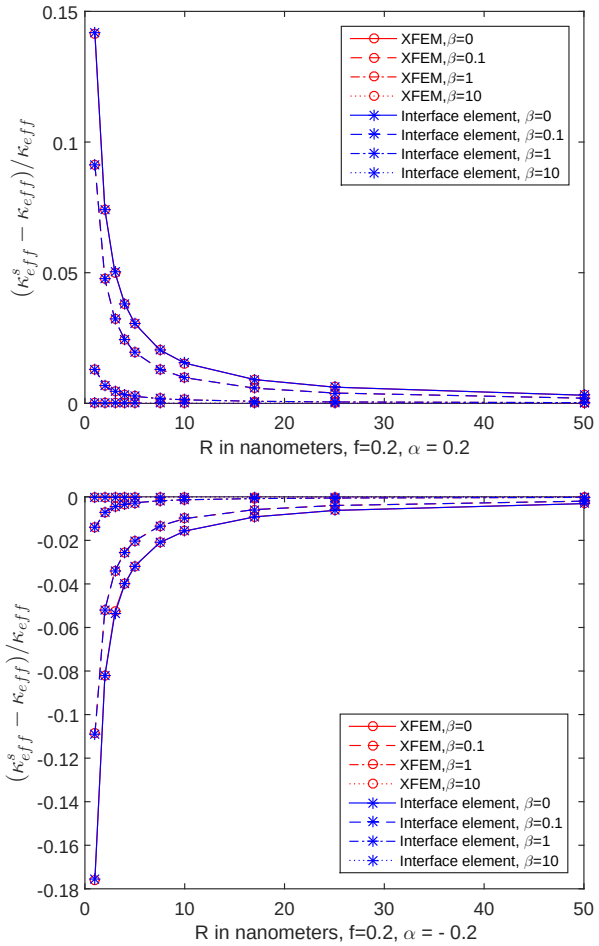

Figure 8: Size dependence of effective plane strain bulk modulus of two-phases materials for $\alpha = 0.2$ and $\alpha = -0.2$ for different values of the stiffness contrast β.

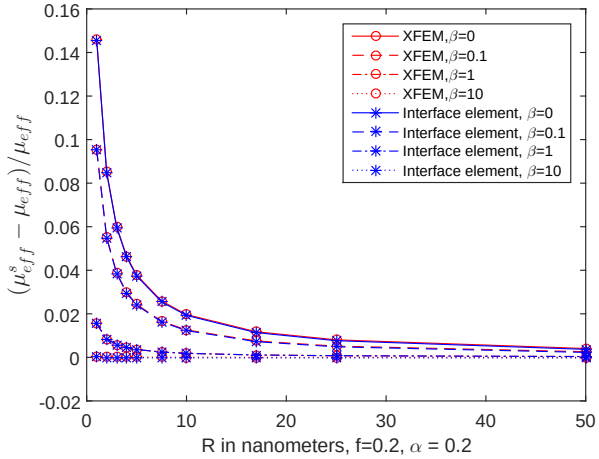

Figure 9: Size dependent of effective plane strain shear modulus of two-phases materials for $\alpha = 0.2$.

4.3. Effective properties of a nanoporous material and influence of the boundary condition

In this subsection, we use the interface parameters obtained through molecular dynamics simulations [35] to compute the effective properties of an aluminum based nanoporous material.

- Aluminum matrix : Young modulus $E = 70$ GPa, Poisson ratio $\nu = 0.32$
- Elastic coherent interface: (given in Miller and Shenoy [35])
  - set A: $\lambda_s = 6.842$ N/m, $\mu_s = -0.375$ N/m.
  - set B: $\lambda_s = 3.48912$ N/m, $\mu_s = -6.2178$ N/m.
  - set C: $\lambda_s = 0$ N/m, $\mu_s = 0$ N/m (no interface elasticity).

We report in the following the results obtained considering different types of boundary conditions on the unit cell represented on the figure 5b namely: Periodic Boundary Conditions (PBC), Kinematic Uniform Boundary Conditions (KUBC), Stress Uniform Boundary Conditions (SUBC). The results obtained with both numerical strategies are compared to the ones obtained from the analytical homogenization strategy denoted as GSCM [16]. The results, for the homogenized bulk moduli, are presented on figure 10 for different values of the radius of void R and different volume fraction f.

We can observe on this figure that, for high volume fractions of nano-voids SUBC and KUBC hypothesis

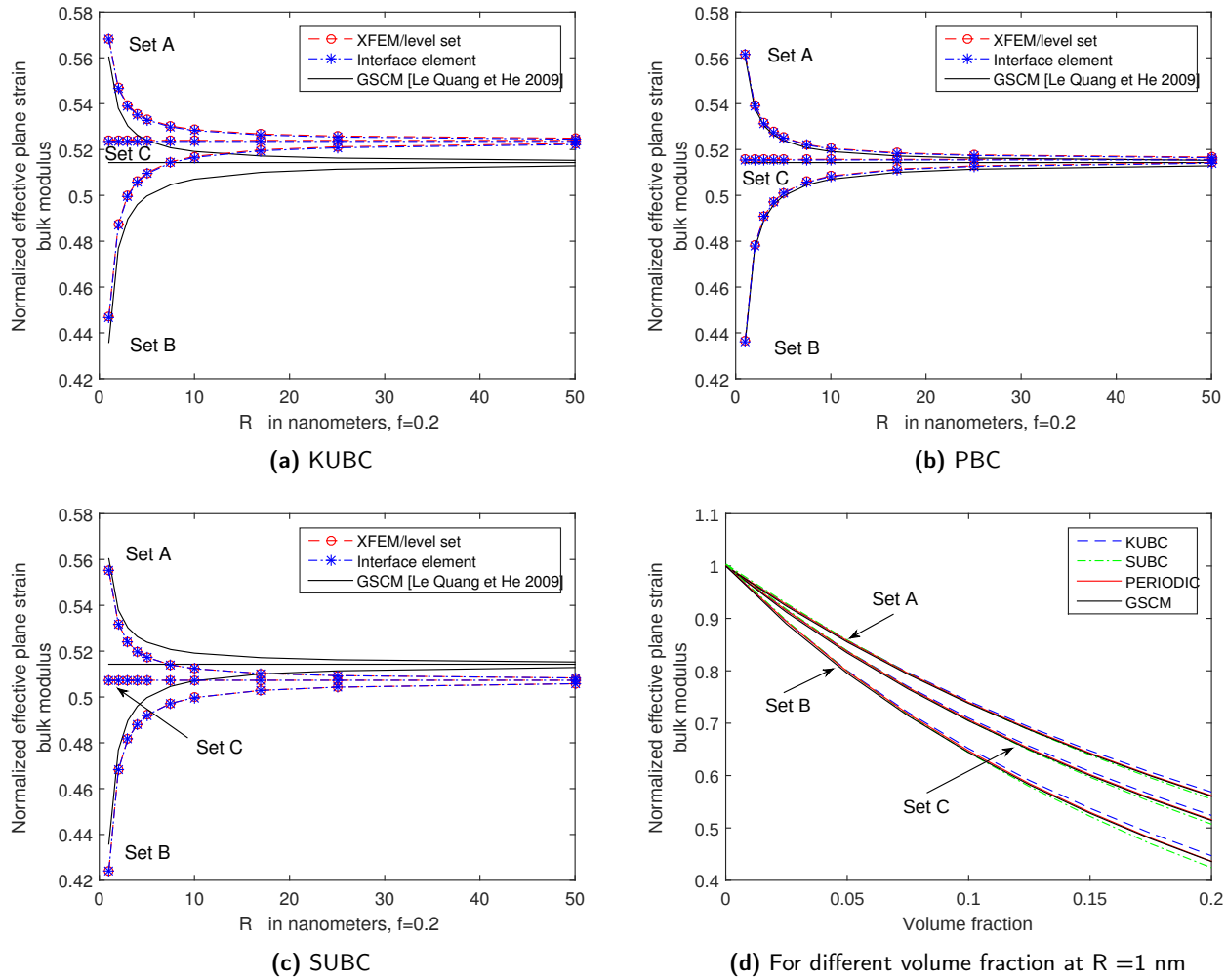

(a) KUBC **(b)** PBC **(c)** SUBC **(d)** For different volume fraction at R =1 nm

Figure 10: Size effect in effective plane-strain bulk modulus for different type of boundary condition.

lead to results quite different from the analytical predictions given in [16]. But, in that comparison of the homogenized bulk modulus, for periodic boundary conditions, the predictions of both numerical strategies are very close to the analytical ones for which cylindrical inclusions in a shell of matrix with a coherent interface, are surrounded by the effective medium. This result for periodic boundary conditions could be explained because the GSCM model takes into account interactions between inclusions and the Periodic Boundary Conditions are better than Kinematic or Stress Uniform Boundary Conditions to account for the interactions between the considered phases, indeed Kinematic and Stress Uniform Boundary Conditions do not take any phase interactions into account. For low volume fraction of nano-voids, numerical and analytical results are very close whatever the boundary conditions.

The same type of comparisons has been carried out considering the effective shear modulus. The results are presented on figure 11. For the Periodic Boundary Condition, a good agreement between the results of the two numerical approaches can be observed on figure 11a, the size dependence of effective shear modulus being clearly shown up. However, unlike the case of bulk modulus, we found a difference between the results of GSCM and the results of numerical homogenization though the periodic boundary conditions still give the closest results (see figures 11b, 11c and 11d).

4.4. Spherical void (axisymmetric model)

The axisymmetric problem is used here to consider spherical nano-inclusions. This model allows us to work on a 2D mesh but handle a symmetric 3D problem. However, the Periodic boundary condition can't be applied to the axisymmetric model. Therefore, only the KUBC and SUBC results are presented (see figure 12). The reference solution is the analytical solution given in [17]. As shown on figure 12, for the bulk modulus, a good agreement between the two presented approaches and between theory and numerical solution is observed. The results for the effective shear modulus are presented on figure 13. Once again, like in the previous subsection, we obtain a difference between nu-

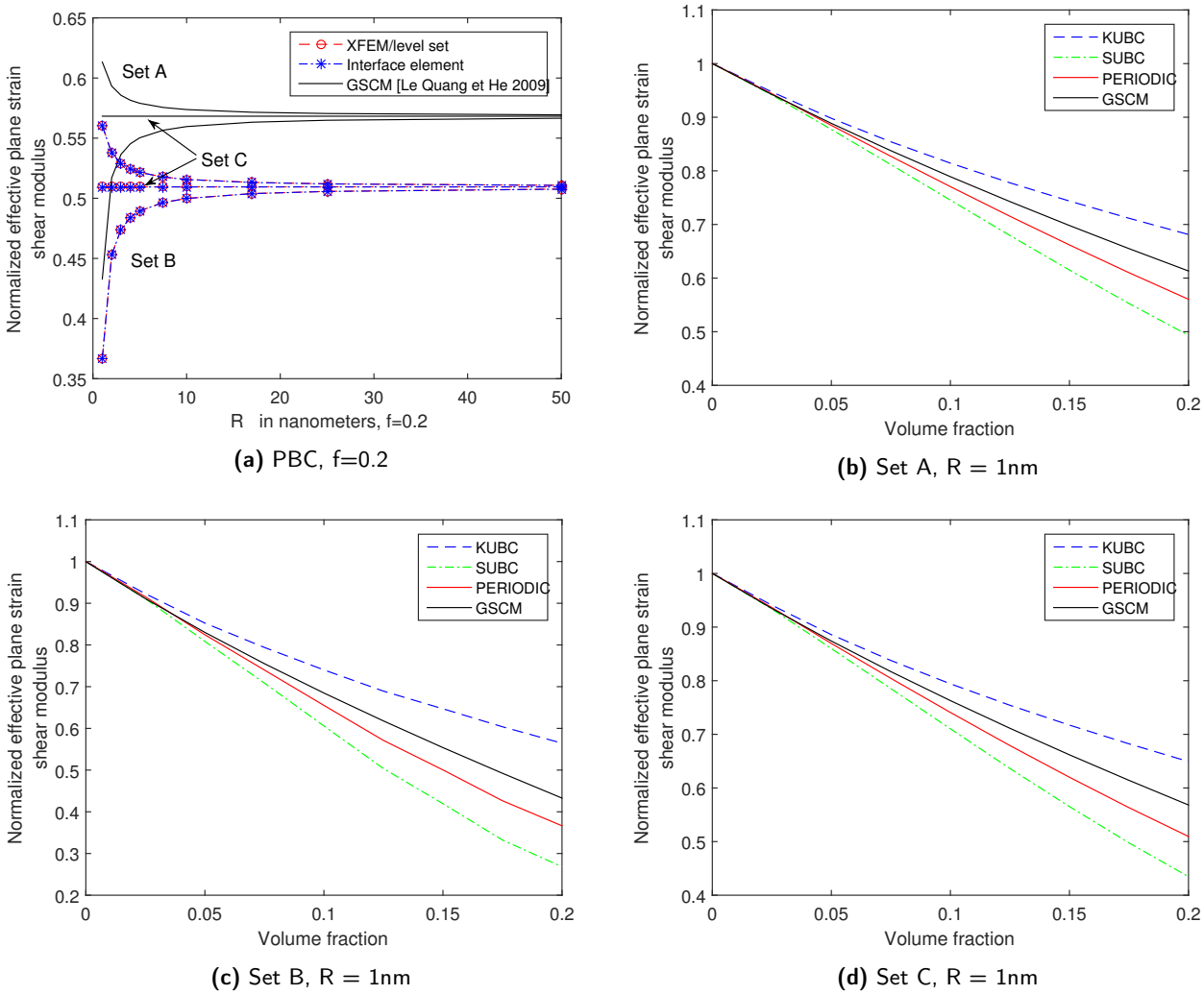

(a) PBC, f=0.2

(b) Set A, R = 1nm

(c) Set B, R = 1nm

(d) Set C, R = 1nm

Figure 11: Size-dependent effective plane-strain shear modulus for different type of boundary condition.

merical and analytical results. However, the size effect is clearly observed and very good agreement between the two considered numerical approaches is obtained.

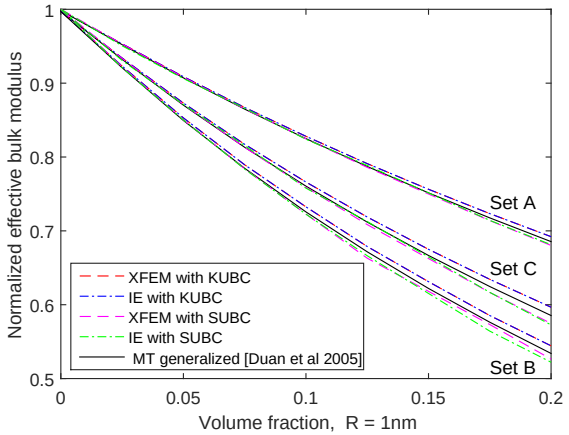

Figure 12: Size-dependent effective bulk modulus with a spherical nanovoid for different type of boundary condition (IE: Interface element; MT: Mori-Tanaka).

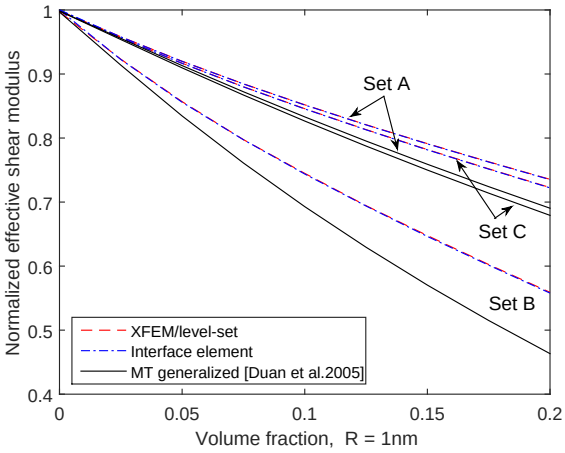

(a) KUBC

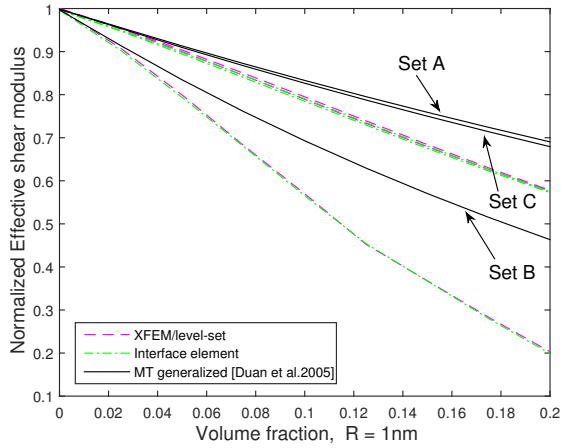

(b) SUBC

Figure 13: Size-dependent effective shear modulus with a spherical nanovoid for different type of boundary condition (MT: Mori-Tanaka).

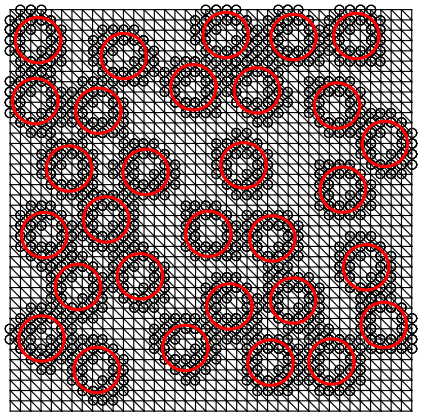

(a) XFEM non-conform mesh

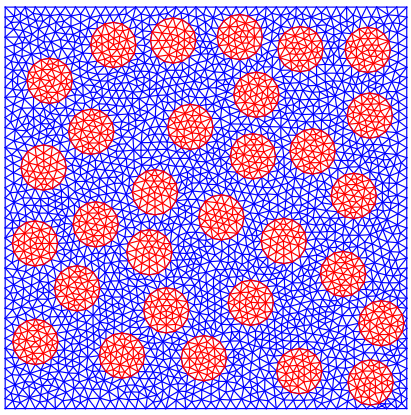

(b) Interface element conform mesh

Figure 14: Two different samples for a 30 randomly distributed nano-voids RVE.

4.5. Nanoporous material with random distribution

In order to complete the comparison between the two considered approaches and to describe more realistic material configurations, we consider a material with randomly distributed nano-voids. Thus a larger RVE composed of 30 circular nanovoids randomly distributed is now considered. Since many voids have to be taken into account in the discretization, the level-set function defined in equation (16) is now computed to the nearest void. The volume fraction is set to 0.3 while we vary the radius of voids. For each radius, a statistical convergence on the mean value of the effective properties is carried out. As shown on figure 15 the convergence needs 15 to 20 samples to be reached. Two different discretizations resulting from two different samples are represented on figure 14.

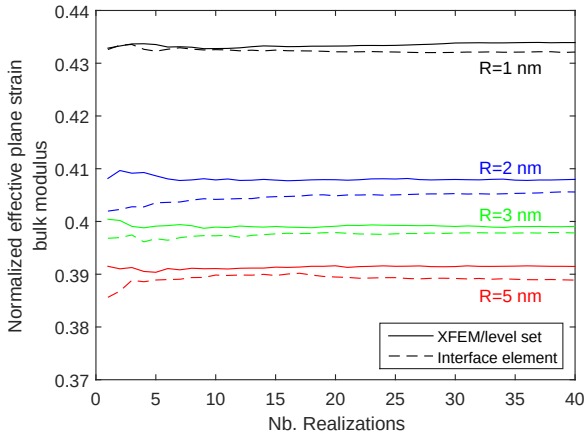

Figure 15: Statistical convergence for $R = 1$ nm, $R = 2$ nm, $R = 3$ nm and $R = 5$ nm.

We used 80x80 nodes meshes for both approaches. The results in term of effective bulk modulus with respect to the size of the nano-voids are presented on figure 16. The influence of the size of nano-voids is clearly observed, although the two approaches don't give exactly the same result. This is probably due to the fact that, as shown in section 4.1, the convergence of XFEM is in presence of surface elasticity slower than the convergence of interface element based method (see figure 6a).

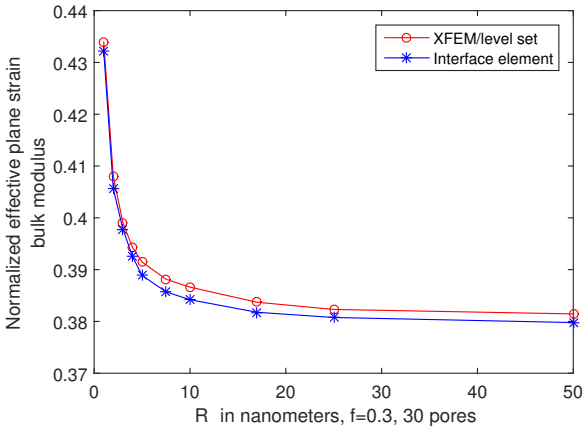

Figure 16: Size effect for effective plane-strain bulk modulus for nanoporous material with randomly distributed nano-voids ($f = 0.3$, $E = 70$ GPa, $\nu = 0.32$, Interface set A).

5. Nonlinear behavior

After the here above presented validation and exploitation for linear behavior, the numerical model is here used in the context of non-linear material behavior. We focus in this section on the very first results given by the two presented approaches. A von Mises type elasto-plastic law with linear isotropic hardening is considered for the bulk with classical yield criterion:

$$f_{(\sigma,q)} = \| \text{dev}(\sigma) \| - \sqrt{\frac{2}{3}}(\sigma_y - q) \, , \tag{36}$$

where σ_y is the elastic limit stress and q is the stress-like variable associated to the hardening variable. The interface is considered as linear elastic. Since we have a non-linear problem, a standard Newton-Raphson procedure and a return mapping integration [36] of elasto-plasticity model have been used. After linearization, at time step $n+1$, Eq. (21) and Eq. (30) now becomes

$$(\mathbf{K}_{n+1} + \mathbf{K}^{\mathbf{s}})\Delta\mathbf{d}_{n+1} = \Delta\mathbf{f}_{n+1} \, , \tag{37}$$

with

$$\mathbf{K}_{n+1} = \int_{\Omega} \mathbf{B}^T \mathbf{C}^{ep}_{n+1} \mathbf{B} d\Omega \, , \tag{38}$$

where $\mathbf{C}^{ep}_{n+1}$ is the coherent tangent matrix [36]. For each iteration of the iterative procedure, we need, at each integration point, to update all the internal variables (for the considered model, we count 5 internal variables: the plastic strain tensor components and the cumulated plastic strain). Hence, for Interface element approach, only 5 variables need to be updated per element, while for XFEM, the iterative procedure for enriched elements requires to compute and update 45 variables per enriched element (see figure 3). In that sense, for complex nonlinear irreversible behaviors, XFEM requires a huge amount of local updatings, each of them resulting from the resolution of local nonlinear equations.

We study the homogeneous behavior of a nanoporous material in terms of the evolution of the mean deviatoric stress with respect to the mean deviatoric part of the strain. Such analysis aims at obtaining the non-linear homogeneized behavior of the composite including surface effect. A simple traction test is performed on the RVE presented on figure 5b with the same material properties as in the previous subsection. The elastic limit stress and hardening modulus of the bulk are set to $\sigma_y = 7$ GPa and $K = 20$ GPa. The homogeneous behavior of the deviatoric part is presented on figure 17. A very good agreement of the results from the two compared numerical approaches is obtained whereas the amount of local nonlinear updating is not of the same order for each method. We can observe the homogeneized behavior of the composite is influenced by the size of the inclusion both in the elastic part (as already shown previously) and in the plastic part of the behavior leading to different elastic limit of the composite. These results are very first results considering nonlinear material behaviors, the non-linearities beeing here limited to the behavior of the matrix. For future works, we could also consider the nonlinear behavior of the interface.

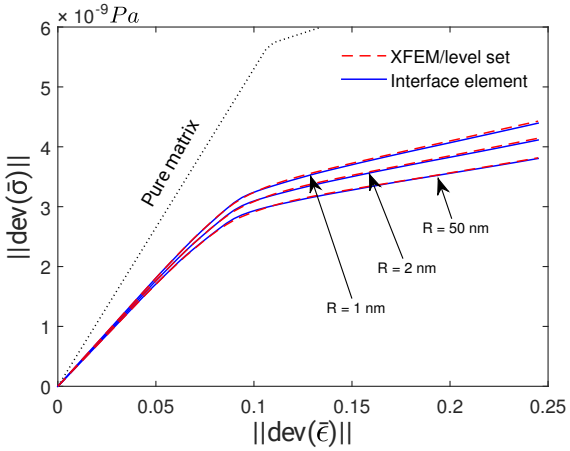

Figure 17: Elastoplastic behavior for three different radius of nano-voids $R = 1$ nm, $R = 2$ nm and $R = 50$ nm.

6. Conclusion

In the context of the prediction of the mechanical behavior of nanocomposites, a comparison of two numerical procedures namely XFEM approach and interface element based strategy has been performed. Both approaches are based on the implementation of a coherent interface with surface elasticity to account for size effect in nanocomposites. The results show that, whatever the contrasts of "rigidity" of the surface with respect to the matrix (coefficient α in this paper) the rate of convergence of XFEM is affected by the presence of surface elasticity while for interface element approach the rate of convergence is not affected. Even so, both of the considered numerical methods are able to reproduce the size effect of the Eshelby problem with coherent interface [12, 13, 14, 15]. Moreover, the performances of the two numerical approaches in reproducing the size effect have also been evaluated for different fictitious materials by varying the contrast of rigidity between the matrix and the inclusions (coefficient β in this paper). The results obtained by the two studied numerical approaches were also compared to micromechanical schemes proposed in [16] and [17] in the context of the evaluation of the effective properties of nanoporous materials. To that purpose, different sets of boundary conditions were considered. As could be expected, due to the underlying hypothesis of the micromechanical model (interactions between inclusions), it emerges that, for the effective bulk moduli, the two numerical approaches estimations are very good agreement with the micromechanical model when considering periodic boundary conditions on the unit cell. However, this is not the case for estimation of the effective shear modulus. To approach more realistic configurations, a material with randomly distributed nano-voids has been considered. The two considered computational approaches give slightly different results in terms of effective properties, which can be attributed to the slower convergence of XFEM compared to the interface element approach. Finally, in order to assess the influence of the non linear behavior of the matrix, a nanoporous unit cell composed of an elastoplastic matrix with linear isotropic hardening and coherent interface has been studied. Those first results allows to envisage to consider more complex non linear behaviors within the numerical homogenization strategy to get closer to more realistic behaviors than linear elastic behaviors for the constituents.

References

[1] Julien Yvonnet, H Le Quang, and Q-C He. An xfem/level set approach to modelling surface/interface effects and to computing the size-dependent effective properties of nanocomposites. *Computational Mechanics*, 42(1):119–131, 2008.

[2] Ali Esmaeili, Paul Steinmann, and Ali Javili. Non-coherent energetic interfaces accounting for degradation. *Computational Mechanics*, 59(3):361–383, Mar 2017.

[3] L. Cauvin, D. Kondo, M. Brieu, and N. Bhatnagar. Mechanical properties of polypropylene layered silicate nanocomposites: Characterization and micro-macro modelling. *Polymer Testing*, 29(2):245 – 250, 2010.

[4] Zvi Hashin. The elastic moduli of heterogeneous materials. *Journal of Applied Mechanics*, 29(1):143–150, 1962.

[5] RM Christensen and KH Lo. Solutions for effective shear properties in three phase sphere and cylinder models. *Journal of the Mechanics and Physics of Solids*, 27(4):315–330, 1979.

[6] Marcin Kamiński. Multiscale homogenization of n-component composites with semi-elliptical random interface defects. *International Journal of Solids and Structures*, 42(11-12):3571–3590, 2005.

[7] Y Benveniste. A general interface model for a three-dimensional curved thin anisotropic interphase between two anisotropic media. *Journal of the Mechanics and Physics of Solids*, 54(4):708–734, 2006.

[8] Sébastien Brisard, Luc Dormieux, and D Kondo. Hashin–shtrikman bounds on the bulk modulus of a nanocomposite with spherical inclusions and interface effects. *Computational Materials Science*, 48(3):589–596, 2010.

[9] Maged Sidhom, Luc Dormieux, and Eric Lemarchand. Poroelastic properties of a nanoporous granular material with interface effects. *Journal of Nanomechanics and Micromechanics*, 5(3):04014001, 2014.

[10] Morton E. Gurtin and A. Ian Murdoch. A continuum theory of elastic material surfaces. *Archive for Rational Mechanics and Analysis*, 57(4):291–323, Dec 1975.

[11] Yu Z Povstenko. Theoretical investigation of phenomena caused by heterogeneous surface tension in solids. *Journal of the Mechanics and Physics of Solids*, 41(9):1499–1514, 1993.

[12] P Sharma and S Ganti. Size-dependent eshelby's tensor for embedded nano-inclusions incorporating surface/interface energies. *Transactions-American society of mechanical engineers journal of applied mechanics*, 71(5):663–671, 2004.

[13] P Sharma, S Ganti, and N Bhate. Effect of surfaces on the size-dependent elastic state of

nano-inhomogeneities. *Applied Physics Letters*, 82(4):535–537, 2003.

[14] P Sharma and S Ganti. Erratum: "Size-Dependent Eshelby's Tensor for Embedded Nano-Inclusions Incorporating Surface/Interface Energies" [Journal of Applied Mechanics, 2004, 71 (5), pp. 663–671]. *Journal of Applied Mechanics*, 72(4):628–628, 2005.

[15] P Sharma, S Ganti, and N Bhate. Erratum: "Effect of surfaces on the size-dependent elastic state of nano-inhomogeneities" [Appl. Phys. Lett. 82, 535 (2003)]. *Applied Physics Letters*, 2006.

[16] H. Le Quang and Q. C. He. Estimation of the effective thermoelastic moduli of fibrous nanocomposites with cylindrically anisotropic phases. *Archive of Applied Mechanics*, 79(3):225–248, Mar 2009.

[17] HL Duan, Jian-xiang Wang, ZP Huang, and Bhushan Lal Karihaloo. Size-dependent effective elastic constants of solids containing nano-inhomogeneities with interface stress. *Journal of the Mechanics and Physics of Solids*, 53(7):1574–1596, 2005.

[18] Sébastien Brisard, Luc Dormieux, and Djimedo Kondo. Hashin–shtrikman bounds on the shear modulus of a nanocomposite with spherical inclusions and interface effects. *Computational Materials Science*, 50(2):403–410, 2010.

[19] Vijay B. Shenoy. Atomistic calculations of elastic properties of metallic fcc crystal surfaces. *Phys. Rev. B*, 71:094104, Mar 2005.

[20] Changwen Mi, Sukky Jun, Demitris A. Kouris, and Sung Youb Kim. Atomistic calculations of interface elastic properties in noncoherent metallic bilayers. *Phys. Rev. B*, 77:075425, Feb 2008.

[21] Vinu Unnikrishnan and J.N. Reddy. Multiscale analysis of the core nanotube in a nanocomposite system. *Finite Elements in Analysis and Design*, 49(1):13 – 18, 2012. Analysis and Design of MEMS/NEMS.

[22] Georgios I. Giannopoulos and Ilias G. Kallivokas. Mechanical properties of graphene based nanocomposites incorporating a hybrid interphase. *Finite Elements in Analysis and Design*, 90:31 – 40, 2014.

[23] Gao Wei, YU Shouwen, and Huang Ganyun. Finite element characterization of the size-dependent mechanical behaviour in nanosystems. *Nanotechnology*, 17(4):1118, 2006.

[24] Qiang Chen, Guannan Wang, and Marek-Jerzy Pindera. Finite-volume homogenization and localization of nanoporous materials with cylindrical voids. part 1: Theory and validation. *European Journal of Mechanics - A/Solids*, 70:141 – 155, 2018.

[25] Qiang Chen, Yu Sun, Guannan Wang, and Marek-Jerzy Pindera. Finite-volume homogenization and localization of nanoporous materials with cylindrical voids. part 2: New results. *European Journal of Mechanics - A/Solids*, 73:331 – 348, 2019.

[26] Niels Saabye Ottosen, Matti Ristinmaa, and Jörn Mosler. Framework for non-coherent interface models at finite displacement jumps and finite strains. *Journal of the Mechanics and Physics of Solids*, 90:124–141, 2016.

[27] Ali Javili, Paul Steinmann, and Jörn Mosler. Micro-to-macro transition accounting for general imperfect interfaces. *Computer Methods in Applied Mechanics and Engineering*, 317(Supplement C):274 – 317, 2017.

[28] Ali Javili, George Chatzigeorgiou, Andrew T. McBride, Paul Steinmann, and Christian Linder. Computational homogenization of nano-materials accounting for size effects via surface elasticity. *GAMM-Mitteilungen*, 38(2):285–312.

[29] Mirza Cenanovic, Peter Hansbo, and Mats G Larson. Cut finite element modeling of linear membranes. *Computer Methods in Applied Mechanics and Engineering*, 310:98–111, 2016.

[30] Mehdi Farsad, Franck J. Vernerey, and Harold S. Park. An extended finite element/level set method to study surface effects on the mechanical behavior and properties of nanomaterials. *International Journal for Numerical Methods in Engineering*, 84(12):1466–1489, 2010.

[31] Q.-Z. Zhu, S.-T. Gu, J. Yvonnet, J.-F. Shao, and Q.-C. He. Three-dimensional numerical modelling by xfem of spring-layer imperfect curved interfaces with applications to linearly elastic composite materials. *International Journal for Numerical Methods in Engineering*, 88(4):307–328, 2011.

[32] DJ Bottomley and T Ogino. Alternative to the shuttleworth formulation of solid surface stress. *Physical Review B*, 63(16):165412, 2001.

[33] N. Moës, M. Cloirec, P. Cartraud, and J.-F. Remacle. A computational approach to handle complex microstructure geometries. *Computer Methods in Applied Mechanics and Engineering*, 192(28):3163 – 3177, 2003. Multiscale Computational Mechanics for Materials and Structures.

[34] Niels Saabye Ottosen, Matti Ristinmaa, and Jörn Mosler. Fundamental physical principles and cohesive zone models at finite displacements–limitations and possibilities. *International Journal of Solids and Structures*, 53:70–79, 2015.

[35] Ronald E Miller and Vijay B Shenoy. Size-dependent elastic properties of nanosized structural elements. *Nanotechnology*, 11(3):139, 2000.

[36] Juan C Simo and Thomas JR Hughes. *Computational inelasticity*, volume 7. Springer Science & Business Media, 2006.